Intermetallics 94 (2018) 138–151

Contents lists available at ScienceDirect

Intermetallics

journal homepage: www.elsevier.com/locate/intermet

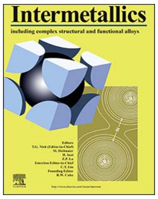

Hot deformation behavior and processing maps of B and Gd containing β-solidified TiAl based alloy

V.S. Sokolovsky[a,*], N.D. Stepanov[a], S.V. Zherebtsov[a], N.A. Nochovnaya[b], P.V. Panin[b], M.A. Zhilyakova[c], A.A. Popov[c], G.A. Salishchev[a]

[a] *Belgorod State University, 85 Pobeda Str., 308015, Belgorod, Russian Federation*
[b] *Federal State Unitary Enterprise "All-Russian Scientific Research Institute of Aviation Materials", 17 Radio Str., 105005, Moscow, Russian Federation*
[c] *Ural Federal University Named After the First President of Russia B.N. Yeltsin, 19 Mira Str., 620002, Ekaterinburg, Russian Federation*

ARTICLE INFO

Keywords:
A. Intermetallics
B. Processing map
C. Dynamic recrystallization
C. Phase transformation
C. Superplasticity

ABSTRACT

High-temperature mechanical behavior and microstructure evolution during hot deformation of an as-cast β-solidified Ti-43.2Al-1.9V-1.1Nb-1.0Zr-0.2Gd-0.2B (at.%) alloy were studied. Phase transformation temperatures and associated phase fields ($\alpha_2 + \gamma$, $\alpha + \gamma$, α, and $\alpha + \beta$) were established by Thermo-Calc calculations, dilatometry, differential scanning calorimetry and microstructure analysis of specimens annealed at different temperatures. The as-cast alloy was subjected to uniaxial compression at temperatures from 900 to 1250 °C and strain rates in the range 0.001–1 s^{-1}. Two temperature intervals with different mechanical behavior were found: the first corresponded to the $\alpha_2+\gamma$ phase field (900–1100 °C), where the microstructure was mainly lamellar, and the second covered the $\alpha + \gamma$, α, and $\alpha + \beta$ phase fields (1100–1250 °C), in which the α phase dominated. In the first interval, mechanical behavior was typical for lamellar structure and was associated with transformation of lamellar structure into globular one via dynamic recrystallization/spheroidization processes. In the second interval, the mechanical behavior was similar despite the changes in phase composition and the controlling process of the microstructure evolution was dynamic recrystallization. In the $\alpha + \gamma$ phase field deformation accelerated the $\gamma \to \alpha$ transformation. Deformation in all phase fields resulted in microstructure refinement which, in turn, induced superplasticity under certain temperature-strain rate conditions. To determine the most suitable conditions for working of the alloy, processing maps were constructed. Two domains with high power dissipation efficiency ($\eta > 0.5$) were found. The first domain was located at the top of the $\alpha_2+\gamma$ and the bottom of the $\alpha+\gamma$ phase fields with the peak efficiency of 0.57 at ~1100 °C and 0.05 s^{-1}. The second domain belonged to the $\alpha + \beta$ phase field with the maximum efficiency of 0.74 at ~1250 °C and 0.5 s^{-1}. The relationships between mechanical behavior and microstructure after deformation were discussed.

1. Introduction

Intermetallic γ-TiAl based alloys are considered as promising materials for aerospace and automotive industries, and potentially can be used for manufacturing of gas turbine blades, turbine rotor discs, and automobile valves due to low density and good high temperature performance [1,2]. However γ-TiAl based alloys have found only limited applications because of low ductility at room temperature and insufficient workability, which makes any thermomechanical processing quite complicated [1,2]. The temperature and strain rate ranges corresponding to the best workability of the alloys can be determined using a processing map [3]; the latter is a product of a superimposition of a power dissipation map and a plastic flow instability map.

The workability of the two-phase γ-TiAl based alloys pronouncedly depends on the percentage of Al [4]. In alloys with less than 45 at. % Al the solidification occurs through the β phase field (β-solidified alloys) [1]. These alloys can consist of the $\alpha_2+\gamma$, $\alpha+\gamma$, α, $\alpha+\beta$ and β phases [5]. If alloys contain more than 45 at. % Al, the solidification occurs through the peritectic reaction $L+\beta \to \alpha$ [1]. The phase diagram of such alloys contain the two-phase ($\alpha_2+\gamma$), ($\alpha+\gamma$) and the single α phase fields [5,6]. In addition both types of the alloys can contain the γ phase; however if in the latter alloys the γ phase exist up to the melting temperature, in the β-solidified alloys this phase can be dissolved at considerably lower temperatures. Accordingly the workability depends on the phase field sufficiently.

Processing maps for the γ-TiAl based alloys with Al > 45 at.% were described in Refs. [6–8]. Deformation behavior was studied for temperatures in the range 800–1300 °C and strain rates between 0.001 and

---

[*] Corresponding author.
E-mail address: sokolovskiy@bsu.edu.ru (V.S. Sokolovsky).

https://doi.org/10.1016/j.intermet.2018.01.004
Received 1 August 2017; Received in revised form 29 December 2017; Accepted 4 January 2018

$10\,s^{-1}$. Domains corresponding to dynamic recrystallization, superplasticity and cracking were identified on the processing maps. These results gave ground for choosing optimal temperature/strain rate conditions of hot working. However it is quite obvious that those data are not applicable to the β-solidified alloys because of completely different sequence and temperatures of the phase transformations during cooling/heating.

Processing maps for the alloys with Al < 45 at.%, for example a lamellar TNM-B_1, were developed in Refs. [9,10]. However, the maps had a limited temperature range covering only three phase fields ($\alpha_2+\beta+\gamma$, $\alpha+\beta+\gamma$, $\alpha+\beta$). The processes which were revealed within those intervals were dynamic recrystallization of either the γ phase in the ($\alpha_2+\beta+\gamma$) phase field or the α phase in the ($\alpha+\beta$) phase field. Meanwhile the β-solidified alloys can also have other phase fields (for instance those which do not contain the β phase [1]), deformation behavior in which has not been studied thoroughly yet. For example the β phase in some β-solidified alloys can dissolve before the eutectoid temperature [11]. The fraction of the γ phase reduces with decreasing the percentage of Al so that the $\gamma \rightarrow \alpha$ phase transformation can be observed during deformation [12]. All aforesaid suggests the need in thorough investigation of β-solidified alloys.

In the present study, the phase transformations, deformation behavior, microstructure evolution and processing map of a novel β-solidifying γ-TiAl based alloy with a nominal composition Ti-43.2Al-1.9V-1.1Nb-1.0Zr-0.2Gd-0.2B [13] were studied in the temperature range of 900–1250 °C and the strain rate range 0.001–1 s^{-1}. The alloy was doped with boron and a rare-earth element (REE) Gd. The addition of boron is expected to result in the formation of borides. Since Gd is a strong oxygen getter and has low solubility in TiAl alloys [14], the formation of oxides and/or Gd-containing intermetallics is anticipated [15]. Together they can reduce the size of lamellar colonies in the as-cast condition [16]. Reducing oxygen content due to REE element can improve ductility of γ-TiAl alloys [17]. The effect of REE on the initial structure, evolution of microstructure and mechanical behavior of β-solidifying alloys during deformation has not been investigated so far.

2. Materials and methods

The ingots measured approximately 225 × 75 × 20 mm^3 were produced by chill casting. The actual chemical composition of the alloy was Ti-43.2Al-1.9V-1.1Nb-1.0Zr-0.2Gd-0.2B-0.358O-0.006C-0.003S-0.007N-0.02H (at.%). The percentage of Ti, Al, V, Nb, Zr, Gd, and B was measured by SEM-based EDS. The concentrations of O, C, S, N, and H were analyzed by the vacuum fusion technique using a LECO PO-316 device. To determine the temperatures of phase transformations, dilatometry (Model DIL 402 C, Netzsch-Gerätebau GmbH, specimens measured 4 × 4 × 20 mm^3) and differential scanning calorimetry (DSC) (SDT Q600 TA Instruments, specimens measured 4 × 4 × 1.5 mm^3) analysis were used. The specimens were cut from the as-cast ingot by electric discharge machine and mechanically polished prior to heating. The measurements were carried out in the temperature range of 25–1450 °C in Ar atmosphere. The phase diagram for the Ti–XAl-1.9V-1.1Nb-1.0Zr-0.031O (X = 35–55; the explanation of the amount of oxygen used for calculations, see Section 3.2) alloys was calculated using a Thermo-Calc software (version TCW5, database TTTIAL). Note that the TTTIAL database does not include Gd and B elements, as well as C, S, N, and H, and therefore they have been omitted during the thermodynamic calculations. For quenching tests specimens measured 10 × 10 × 15 mm^3 were cut from the as-cast ingot, heated in a Nabertherm furnace to 1100–1250 °C for 10 or 120 min in laboratory air and then water quenched.

Cylindrical specimens measured 10 mm in diameter and 15 mm in height were compressed isothermally to a true strain of 1.2 at constant strain rates of 0.001, 0.01, 0.1, and 1.0 s^{-1} and temperatures of 900, 950, 1000, 1050, 1100, 1150, 1200, and 1250 °C. The phase fields corresponding to the temperatures of the mechanical testing were established based on the experimentally measured phase transformation temperatures. An Instron 300LX hydraulic universal testing machine equipped with a radial heating furnace was used for the compression tests in the temperature range of 900–1050 °C in laboratory air. The specimens were held at the required temperature for 10 min before the start of the test and then water quenched after the compression. A Gleeble 3800 thermo-mechanical machine was used for the tests at 1100–1250 °C. The specimens were induction heated by 10 °C per second and then soaked for 5 min at the test temperatures in vacuum (10^{-4} bar) before the compression. After the strain the specimens were quenched by argon gas flow. Cooling rates were sufficient to fix a high-temperature structure of the alloy. The deformed specimens were sectioned along the compression axis. The microstructure of the compressed specimens was examined in central (most deformed) area. The lateral surfaces which endured the maximum tensile stresses during the compression test were analyzed to discover surface cracks.

The microstructure was examined using scanning electron microscopy (SEM), electron backscattered diffraction (EBSD) and transmission electron microscopy (TEM). The specimens for the SEM analysis were mechanically polished. The SEM investigations were carried out using a FEI Quanta 600 FEG (field emission gun) microscope in a backscattered electron (BSE) mode; the microscope was equipped with an energy-dispersive (EDS) detector. The volume fraction of the phases was calculated in accordance with ASTM E562-11 [18]. The volume fraction and the size of spheroidized/recrystallized grains in temperature interval 900–1100 °C were calculated using SEM images.

A FEI Nova NanoSEM 450 scanning electron microscope operated at 30 kV and equipped with a Hikari EBSD detector was used to obtain EBSD maps. The EBSD measurements were carried out using the TSL Data Collection ver. 6.2 software. The step size of the EBSD scan was varied from 100 nm to 0.5 μm depending on the grain size. Each EBSD map comprised at least 1000 grains. The α-Ti (Pearson symbol hP8; space group P63/mmc № 194; a = 0.5752 nm, c = 0.4657 nm) and the TiAl (Pearson symbol tP2; space group P4/mmm № 123; a = 0.4020 nm, c = 0.4077 nm) phases were selected as possible phases during scanning. The fractions of low-angle boundaries (LABs) ($2 \leq \theta < 15°$) and high-angle boundaries (HABs) ($\theta = 15°$) were calculated from the EBSD maps. The fraction of recrystallized grains was determined from grain orientation spread (GOS) maps [19]. In the present work, the GOS cut–off value of 1° was used to distinguish dynamically recrystallized grains (i.e. with the GOS < 1°). This value was chosen on the basis of numerous EBSD misorientation measurements within recrystallized grains.

Samples for the TEM analysis were first mechanically ground to ~100 μm thickness and then electro-polished in a mixture of 5% perchloric acid, 35% butanol and 60% methanol at 27 V and −32 °C using a twin-jet TenuPol-5 Struers. The TEM investigations were carried out using a JEOL JEM - 2100 microscope operated at 200 kV and equipped with an EDS detector. Selected area electron diffraction patters (SAEDs) were used to identify the constitutive phases in TEM examination. The Digimizer software was used for the analysis of the SAEDs. The reference lattice parameters of the phases were taken from NIMS Materials Database [20].

The concept of using processing maps to determine the best workability conditions (temperature and strain rate) was given in Ref. [3]. The strain rate sensitivity of flow stress (*m*) is a parameter that indicates how the energy which applied during deformation shares between heat and microstructural changes:

$$m = \frac{\Delta \log \sigma}{\Delta \log \dot{\varepsilon}}, \tag{1}$$

where σ is the flow stress and $\dot{\varepsilon}$ is the strain rate.

The efficiency of power dissipation (η) of a work piece can be obtained by comparing its power dissipation through microstructural changes with that occurring in an ideal linear dissipator (m = 1) [3]:

$$\eta = \frac{m/(m+1)}{1/2} = \frac{2m}{m+1}, \tag{2}$$

The power dissipation map represents the projection of a three-dimensional surface describing the variation of η with temperature and strain rate on the $T - \dot{\varepsilon}$ plane. In addition a criterion for the onset of flow instability during hot deformation ξ was determined in terms of nonequilibrium thermodynamics with respect to plastic flow in continuum mechanics [3] as:

$$\xi(\dot{\varepsilon}) = \frac{\partial ln(m/m+1)}{\partial ln\dot{\varepsilon}} + m \tag{3}$$

The variation of dimensionless parameter $\xi(\dot{\varepsilon})$ with temperature and strain rate constitutes an instability map. In this map microstructure instability occurs when temperature and strain rate regimes result in $\xi < 0$. The flow instability is usually related to adiabatic shear bands formation, flow localization, dynamic strain aging, mechanical twinning and kinking or flow rotations [3]. A superimposition of the instability map on the power dissipation map results in a processing map, which reveals domains where the workability of the alloy is high (domains where, for example, dynamic recrystallization (DRX) or superplasticity (SP) occur) and the limiting conditions for the regimes of flow instability. The best workability of the material can be achieved when the processing is carried out under conditions of highest efficiency in the "safe" domains avoiding the regimes of flow instabilities [3].

3. Results

3.1. Initial microstructure

The microstructure of the as-cast Ti-43.2Al-1.9V-1.1Nb-1.0Zr-0.2Gd-0.2B was found to consist mainly of $\alpha_2+\gamma$ lamellae colonies surrounded by particles of various chemical compositions (the γ phase, the β phase, two types of Gd-rich phases and two types of borides, Fig. 1). The size of the $\alpha_2+\gamma$ colonies was approximately 20 μm (Fig. 1a) with the average inter-lamellar spacing of 70 nm (Fig. 1c). The Gd-rich particles of 160–370 nm in size were identified by the SAED patterns analysis as Gd_2TiO_5 or $GdAl_3$. These particles were homogeneously distributed within the lamellar colonies (Fig. 1b, h, i). However the size of the Gd_2TiO_5 and $GdAl_3$ particles located in between the $\alpha_2+\gamma$ colonies was found to be much larger, attaining 2–5 μm (Fig. 1a and g). The chemical composition of the Gd-rich particles is shown in Table 1. Most likely the obtained amount of oxygen in the Gd oxides (36–37 at.% according to EDS) was underestimated due to poor sensitivity of EDS systems to light elements. However, using the stoichiometric concentration of oxygen in the oxide, the volume fraction of the oxide particles (0.5%), densities of the alloy (4.153 g/cm^3) and the oxide (6.105 g/cm^3) the amount of oxygen presented in the alloy (excepting the Gd_2TiO_5 phase) can be estimated as 0.031 at.%, thereby suggesting a considerable decrease in the content of solved oxygen in the alloy due to Gd.

In contrast to the nearly equiaxed oxide and aluminide particles, TiB and TiB_2 borides had a platelet morphology with the thickness of laths of 100–250 nm (Fig. 1e and f). They predominantly were heterogeneously distributed at boundaries of the colonies. The total volume fraction of the Gd-rich particles and borides did not exceed 2%.The γ and β phases were mainly found as thin interlayers between some colonies of the $\alpha_2+\gamma$ lamellae; the thickness of the γ and β phases was 0.5–1.5 and 0.3–1.2 μm, respectively (Fig. 1c and d). The β phase contained very fine (10–20 nm) precipitates of the ω-phase (Fig. 1d). The total volume fraction of the γ and β phases was close to 1%.

3.2. Phase transformations

A phase diagram for the Ti–Al-V-Nb-Zr-O system alloys was calculated using the Thermo-Calc software for constant concentrations of V, Nb, Zr, O (1.9, 1.1, 1.0 and 0.031 at.%, respectively) and variable percentages of Al in the range from 35.0 to 55.0 at.% (Fig. 2, Table 2). The estimated concentration of oxygen in the alloy (excepting the Gd_2TiO_5 oxide, see the previous section) was used for the calculations since the melting temperature of the oxides is higher than the melting temperature of the alloy [21]. Note that the available commercial thermodynamic database for TiAl-based alloys (TTTIAL) does not include Gd and B, as well as other impurities. Therefore the effect of these elements on phase transformations cannot be estimated using the thermodynamic calculations. The sequence of the phases which form in the Ti-43.2Al-1.9V-1.1Nb-1.0Zr-0.2Gd-0.2B alloy during cooling from the liquid state included the β, α, γ, and α_2 phases. Temperatures of the formation of these phases are denoted at the phase diagram as T_β, T_α and $T\gamma$, respectively. The eutectoid reaction temperature at which $\alpha \rightarrow \alpha_2+\gamma$ transformation occurred is denoted as T_e. The fraction of the γ phase at T_e was ~50% according to the Thermo-Calc calculations.

The calculated temperatures of the phase transformations were compared with the experimental results obtained by dilatometry and DSC (Table 2). The experimental phase transformation temperatures (i.e. T_e, T_γ, T_α and T_β) obtained by two different experimental methods are very close (Table 2). Note that both dilatometry and DSC show a peak corresponding to the temperature of dissolution of the ω phase (T_ω) (Table 2). The determined T_ω is close to that for another γ-TiAl alloy Ti–43.5Al–4Nb–1Mo–0.1B [22]. The experimental phase transformation temperatures (Table 2) were used further to determine the phase fields.

Significant differences between the calculated and experimental phase transformation temperatures should be mentioned. For instance, the value of T_α predicted by the ThermoCalc software was ~215–234 °C higher than the experimental temperatures (Table 2). The difference can be associated with variations in chemical compositions (i.e. absence of Gd, B and impurities in the calculations) of the alloys which were used for the calculations and experimental studies by dilatometry/DSC. However the concentrations of impurities (C, S, N, and H) are insignificant while Gd and B were mostly found in the stable oxide, aluminide and borides particles (Fig. 1). Therefore these factors were unlikely to affect the phase transformation temperatures considerably. Possibly the underestimated content of oxygen in the alloy (0.031 at.%) could not result in a decrease in the value of T_α since oxygen is known to be a strong α-stabilizer. In addition, the thermodynamic modeling produces an equilibrium phase diagram, while the experiment is always conducted under non-equilibrium conditions. Therefore even all together all these factors are unlikely to result in such a big difference in the predicted and experimental results. Most probably, the observed difference can be associated with the lack of credibility of the commercial thermodynamic database for the present set of alloying elements and their concentrations. Note that considerable differences between the results of ThermoCalc calculations and experimental data on phase transformations for different γ-TiAl based alloys have been already reported by several authors [23,24].

Further insight into the phase transformations of the alloy was obtained by annealing at temperatures of 1100, 1150, 1200 and 1250 °C for 2 h in air atmosphere following by water quenching for preserving high-temperature microstructures (Fig. 3). Annealing in the $\alpha_2+\gamma$ phase field (1100 °C) resulted in the formation of a colony $\alpha_2+\gamma$ microstructure with a very heterogeneous distribution of the interlamellar spacing which varies from ~0.2 to 1 μm (Fig. 3a) in different colonies. The β phase was not detected in the microstructure after annealing at 1100 °C. Spheroidized particles of the γ phase measured ~2.5 μm in diameter were found between $\alpha_2+\gamma$ colonies (Fig. 3a). The volume fraction of the γ phase was ~40%. At 1150°C ($\alpha+\gamma$ phase field) the γ phase lamellae began to dissolve and after 2 h annealing some colonies were found to be almost free of lamellae (Fig. 3b). The volume fraction of the γ phase decreased to 25%. After annealing at 1200 °C (α-phase field) for 2 h the microstructure consisted of equiaxed α grains measured ~50 μm in diameter (Fig. 3c). Annealing in the $\alpha+\beta$ phase field

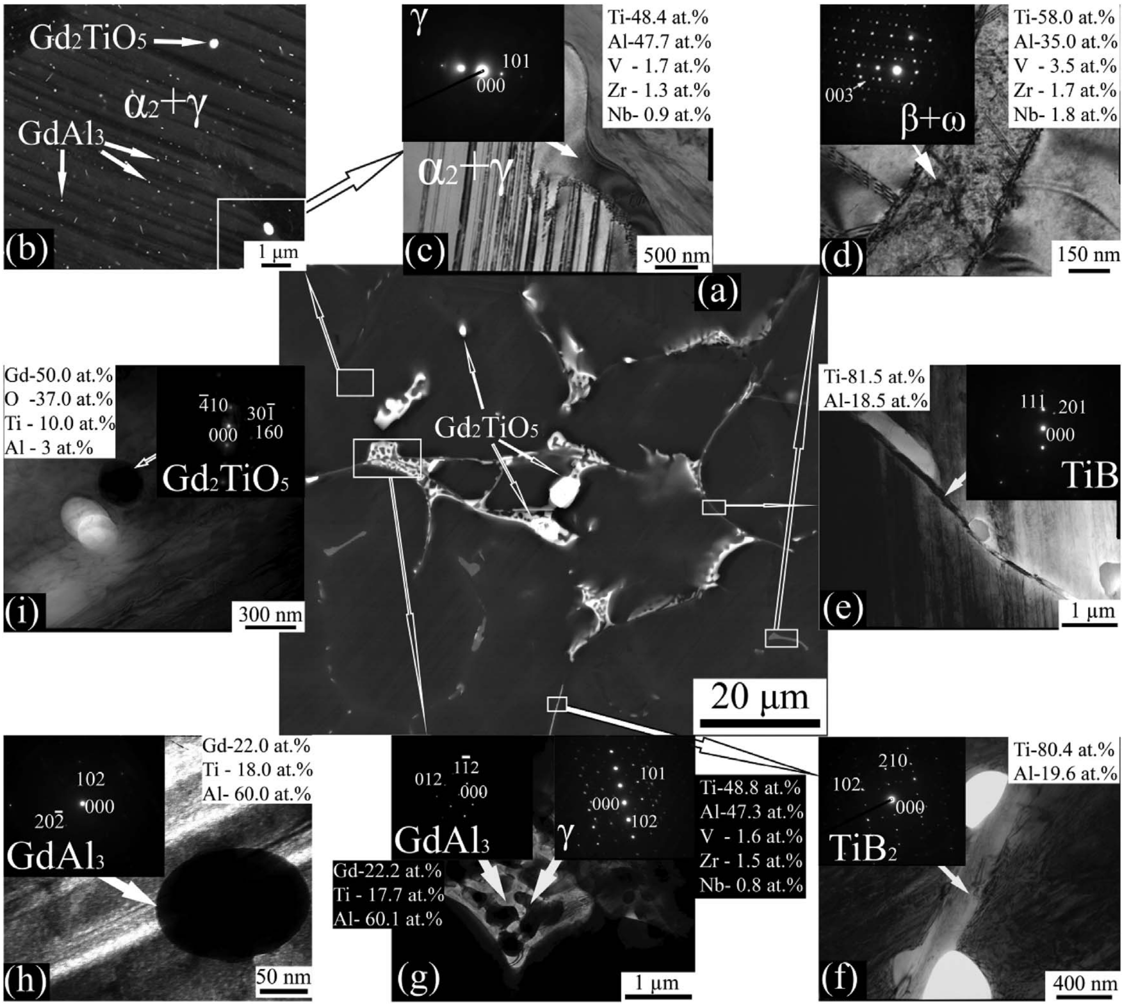

Fig. 1. Microstructure of the as-cast Ti-43.2Al-1.9V-1.1Nb-1.0Zr-0.2Gd-0.2B alloy: (a) overview at low magnification; (b) Gd_2TiO_5 and $GdAl_3$ phases particles distributed within a colony of $\alpha_2+\gamma$ lamellae; (c) a layer of the γ phase between $\alpha_2+\gamma$ colonies; (d) precipitations of the ω phase in a β lamella; (e) a TiB layer between $\alpha_2+\gamma$ colonies; (f) a TiB_2 lath between $\alpha_2+\gamma$ colonies; (g) nearly equiaxed $GdAl_3$ and γ phases particles at a boundary between $\alpha_2+\gamma$ colonies; (h) a particle of the $GdAl_3$ phase inside a $\alpha_2+\gamma$ colony; (i) a particle of the Gd_2TiO_5 phase inside a $\alpha_2+\gamma$ colony; (a, b) SEM-BSE images; (c–i) bright-field TEM images. SAED patterns and chemical composition are shown for the corresponding precipitates.

Table 1
Chemical composition of the Gd_2TiO_5 and $GdAl_3$ phases determined by the SEM- and the TEM-based EDS-analysis in the as-cast Ti-43.2Al-1.9V-1.1Nb-1.0Zr-0.2Gd-0.2B alloy.

Element, at.%		Gd	Ti	Al	O
Gd_2TiO_5	SEM	50	10	3	37
	TEM	41	9	14	36
$GdAl_3$	SEM	27	23	50	0
	TEM	22	18	60	0

(1250 °C) gave rise to the formation of 2 µm thick laths of the β phase along α/α grain boundaries (Fig. 3d). The average size of the α grains was found to be ~35 µm. The effect of soak time at a given temperature was estimated comparing samples annealed for 10 min (the images are not presented) and 2 h (Fig. 3). No principal difference was found; yet the microstructure of the alloy tended to become coarser at higher annealing times. More detailed information on this issue can be found in Section 3.4. It should be also particularly noted that the shape, location and the size of the Gd-rich phases and borides particles did not change noticeably during annealing within the whole studied temperature interval (1100–1250 °C) (Fig. 3).

3.3. Mechanical behavior

Stress-strain curves of the Ti-43.2Al-1.9V-1.1Nb-1.0Zr-0.2Gd-0.2B alloy obtained during isothermal compression at 900–1250 °C showed stress peak at the beginning of plastic flow followed by a flow softening and a steady state flow stage (Fig. 4) that is quite typical of high temperature deformation of such kind of materials [9,25]. The flow stress of the alloy expectably decreased with increasing temperature and decreasing strain rate. In addition the length of the steady state flow stages became greater at higher temperatures. At low temperatures and high strain rates some specimens fractured before attaining the target deformation $\varphi = 1.2$ (Fig. 4a–e). Specimens fracture or cracking was observed in the $\alpha_2+\gamma$ phase field at all studied temperatures (except 1100°C) and strain rates $> 0.001\ s^{-1}$. In the $\alpha+\gamma$ (1150°C), α (1200°C) or $\alpha+\beta$ (1250°C) phase fields the specimen cracking occurred only at the maximum strain rate ($1\ s^{-1}$). Flow stress oscillations, which were observed at temperatures ≥1150 °C and a high strain rate (Fig. 4f–h), can be associated with dynamic recrystallization [26].

3.4. Microstructure evolution during hot deformation

Microstructure of the alloy compressed to $\varphi = 1.2$ depended considerably on deformation temperature and strain rate (Figs. 5–11). Deformation in the temperature interval 900–1100°C ($\alpha_2+\gamma$ phase

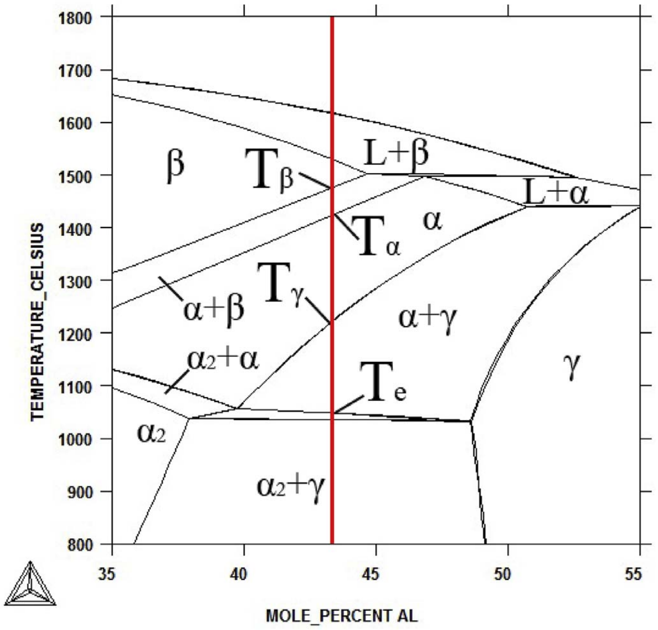

Fig. 2. Phase diagram of the Ti–XAl-1.9V-1.1Nb-1.0Zr-0.031O (X = 35–55) system alloys calculated by Thermo-Calc software.

Table 2
The calculated temperatures of the phase transformations in the Ti–43.2Al-1.9V-1.1Nb-1.0Zr-0.031O alloy and the experimental results for the Ti-43.2Al-1.9V-1.1Nb-1.0Zr-0.2Gd-0.2B alloy.

Method	Temperature of phase transformation, °C				
	T_ω	T_e	T_γ	T_α	T_β
Calculated	–	1044–1054	1219	1435	1482
Dilatometry	770	1115–1125	1182	1201	1435
DSC	830	1109–1132	1180	1220	1420

field) (Figs. 5, 6a–d) resulted in transformation of the initial $\alpha_2+\gamma$ lamellae microstructure into equiaxed α_2 and γ phase particles [27–29]. The lamellae transformation occurred due to the development of a recrystallization/spheroidization processes. The volume fraction and the size of the spheroidized/recrystallized grains increased with an increasing deformation temperature and decreasing strain rate (Figs. 5, 6a–d, 10a and b).

More homogeneous fine-grained structure formed at 1100 °C and 0.001 s^{-1} due to more complete spheroidization/recrystallization processes (Fig. 6c and d). An increase in a strain rate led to the formation of a partially spheroidized/recrystallized microstructure which was consisted of elongated remnants of initial colonies aligned with plastic flow direction, and fine-grained areas (Fig. 6a and b). The homogeneity of the gamma particles distribution was also higher at the lowest strain rate of 0.001 s^{-1} (Fig. 6d) in comparison with 1 s^{-1} (Fig. 6b). The size of spheroidization/recrystallization grains which was obtained during deformation decreased with an increase in strain rate from 5 μm (at $\dot{\varepsilon}$ = 0.001 s^{-1}) to 0.8 μm (at $\dot{\varepsilon}$ = 1 s^{-1}) at T = 1100°C (Fig. 10b). The size of new grains at lower temperatures was not determined because of uncompleted spheroidization/recrystallization processes.

During deformation in the $\alpha+\gamma$ phase field (1150°C) the lamellar microstructure was transformed into equiaxed one (Figs. 3b and 6e, g). However the homogeneity of the microstructure depended on strain rate considerably. At a high strain rate of $\dot{\varepsilon}$ = 1 s^{-1} a heterogeneous elongated microstructure formed with coarse particles of the γ phase (Fig. 6e and f). A decrease in strain rate led to some elongation of the α grains along the plastic flow direction with a pronounced reducing in the fraction of the γ phase (Fig. 6g and h). The microstructure consisted both elongated large and equiaxed small grains. The grain size increased from 13.5 μm at $\dot{\varepsilon}$ = 0.001 s^{-1} to 1.5 μm at $\dot{\varepsilon}$ = 1 s^{-1} (Fig. 10b). It is well known that the kinetics of the γ→α (or $\gamma\rightarrow\alpha_2$ [12]) phase transformation in a γ-TiAl alloys is quite slow; however it can be considerably promoted by strain [30]. Static annealing for 2 h at T = 1150°C resulted in the volume fraction of the γ phase Vγ = 25% (Fig. 3b), while compression to φ = 1.2 at the same temperature and a strain rate of 0.001 s^{-1} (deformation took ~15 min in this case) left only 2% of the γ phase (Fig. 7). Besides, the volume fraction of the γ phase increased with increasing strain rate; for instance, after deformation at 1150 °C and 1 s^{-1} the value of Vγ was found to be 15% (Fig. 7).

The effect of strain level on the volume fraction of the γ phase is clearly seen from the analysis of microstructure in different areas of a specimen, compressed to φ = 1.2 at 1150°C and 0.001 s^{-1} (Fig. 8a). The volume fraction and morphology of the γ phase in the central (Fig. 8b) and edge (Fig. 8c) regions were found to be considerably different from each other due to the different level of strain. The volume fraction of the nearly equiaxed γ particles was less than 2% in the central region while the microstructure of the edge regions consisted ~10% of the lamellar γ. This finding clearly indicates that the γ→α transformation is accelerated by deformation.

An increase in deformation temperature to the α or $\alpha+\beta$ phase fields (1200 and 1250 °C, respectively) resulted in a homogeneous refined microstructure even at high strain rates (Fig. 9). Some heterogeneity can only be observed at T = 1200°C and a strain rate of $\dot{\varepsilon}$ = 1 s^{-1} (Fig. 9a); in all other cases within the studied temperature - strain rate interval a highly uniform microstructure was formed (Fig. 9b–h). An increase in deformation temperature from 1200 °C to 1250 °C resulted in microstructure coarsening at all strain rates (Fig. 9). At low strain rates of 0.001–0.01 s^{-1} and temperature of 1250 °C curved grain boundaries were observed (Fig. 9g and h).

The grain size which was obtained during deformation decreased with an increase of a strain rate from 19.5 μm (at $\dot{\varepsilon}$ = 0.001 s^{-1}) to 3.3 μm (at $\dot{\varepsilon}$ = 1 s^{-1}) at T = 1200°C and from 23.5 μm (at $\dot{\varepsilon}$ = 0.001 s^{-1}) to 4.1 μm (at $\dot{\varepsilon}$ = 1 s^{-1}) at T = 1250°C (Fig. 10b). It worth noting that the average size of the α grains just before deformation (10 min soak at the deformation temperatures) was 32 or 31 μm at 1200 or 1250 °C, respectively. A weak effect of temperature and soak time (after 2 h at 1250 °C the grain size increased to 35 μm only, see section 3.2) on the α grains growth in the latter case was most likely associated with a constraint effect from the β phase which existed in the $\alpha+\beta$ phase field in the form of thin interlayers between the α grains (Fig. 3d). Much more pronounced grain growth from 32 μm (10 min) to ~50 μm (2 h) was observed during soaking at 1200 °C (the α phase field). These results show that grain growth during deformation at 1250 °C and $\dot{\varepsilon}$ = 0.001 s^{-1} is retarded by the β phase particles.

Dependencies of the volume fraction of recrystallized grains (i.e. grains with the grain orientation spread, GOS < 1°) and the HAGBs fraction on deformation temperatures (1150–1250 °C) and strain rates (0.001–1 s^{-1}) are shown in Fig. 11. In the $\alpha+\gamma$ phase field (T = 1150 °C) at a strain rate of 0.001 s^{-1} the fraction of the recrystallized grains was ~30% (Fig. 11a). An increase in strain rate resulted in an increase in fraction of grains with the GOS < 1° to the maximum (~72%) at $\dot{\varepsilon}$ = 0.1 s^{-1}. At even higher strain rate, a moderate decrease in the recrystallized fraction to ~63% was found. In the α phase field (T = 1200 °C) an increase in strain rate also resulted in an increase in the volume fraction of the recrystallized grains (Fig. 11a). The peak value of ~80% was attained at $\dot{\varepsilon}$ = 0.1 s^{-1}. In the $\alpha+\beta$ phase field (T = 1250 °C) the highest fraction of grains with the GOS < 1° (97%) was found at the lowest strain rate of 0.001 s^{-1}. At higher strain rates, the fraction of the recrystallized grains became lower (70–75%). This is an indication of diminishing of dynamic recrystallization at high temperatures. In the $\alpha+\gamma$ and α phase fields the HABs fraction increased with an increase in strain rate and reached the maximum at 0.1 s^{-1} (Fig. 11b), similarly to the fraction of grains with the GOS < 1°

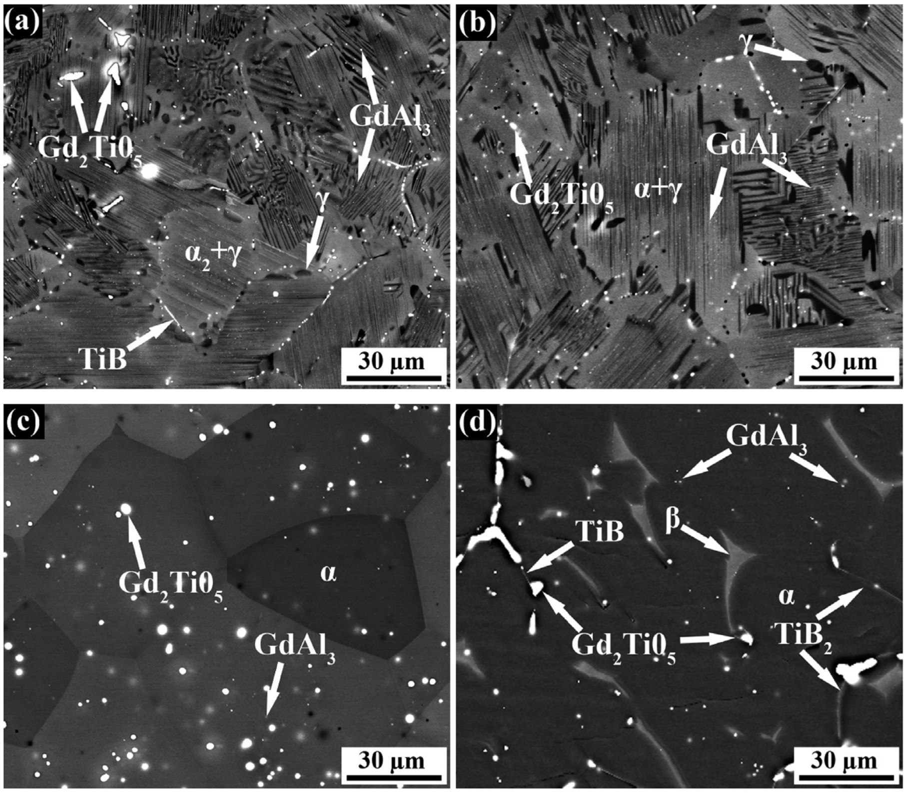

Fig. 3. Microstructure of the Ti-43.2Al-1.9V-1.1Nb-1.0Zr-0.2Gd-0.2B alloy after annealing for 2 h in laboratory air at: (a) 1100 °C ($\alpha_2+\gamma$ phase field); (b) 1150 °C ($\alpha+\gamma$ phase field); (c) 1200 °C (α-phase field) or (d) 1250 °C ($\alpha+\beta$ phase field) and water quenching.

(Fig. 11a). In the $\alpha+\beta$ phase field (T = 1250 °C) the HABs fraction at a strain rate of 0.001 s^{-1} was ~90%. The HABs fraction slightly reduced with an increase in strain rate.

Close examination also showed that the lath morphology of the β phase has preserved even after deformation to φ = 1.2 at T = 1250 °C and $\dot{\varepsilon}$ = 0.001 s^{-1} (Fig. 12a). The β phase existed in the microstructure as a network of thin (~0.2 µm) interlayers which divides particles of the α phase. In addition elongated particles of the Gd_2TiO_5 (measured ~100 × 400 nm, Fig. 12a, d) and $GdAl_3$ (~10–20 nm, Fig. 12b and c) can be seen in the β phase or in the α/β and α/α boundaries (Fig. 12b–d).

At all deformation temperatures cracks were arisen at the side faces of the specimens. Microstructure examination revealed that the cracks/pores formed along some colony/grain boundaries (Fig. 13) most probably due to strain localization. The morphology of these defects depended on deformation temperatures. Within the same $\alpha_2+\gamma$ phase field thin and long cracks along colony boundaries were observed at lower temperatures (i.e. 900 °C, Fig. 13a), while round pores arranged in chains were found at 1100 °C. Similar chains of pores were observed after deformation at 1150 °C (Fig. 13c). At 1250 °C and 1 s^{-1} larger size pores appeared at boundaries between grains of the α phase (Fig. 13d).

3.5. Processing map analysis

Processing maps for strains φ = 0.2, 0.5 and 0.7, temperatures T = 900–1250 °C and strain rates $\dot{\varepsilon}$ = 0.005–0.5 s^{-1} are shown in Fig. 14. The strain rate sensitivity of flow stress (*m*) values was used for the processing maps plotting (Table 3). It is seen that the maximum values of *m* were observed at the top of the $\alpha_2+\gamma$ phase field (m = 0.33–0.4 at T = 1100 °C and $\dot{\varepsilon}$ = 0.005–0.05 s^{-1}) and the $\alpha+\beta$ phase field (m = 0.46–0.59 at 1250 °C and $\dot{\varepsilon}$ = 0.05–0.5 s^{-1}). A decrease in a strain rate can both increase (for example at T = 1100 °C and 1150°C and φ = 0.5 or 0.7) or decrease (at T = 1250°C and φ = 0.5 or 0.7) the value of *m*.

An increase in the power dissipation efficiency η with increasing the values of *m* accords pretty well with Eq. (2) resulting in the formation of two domains with $\eta > 0.5$ on the processing maps at each strain level (Fig. 14). On the processing map for φ = 0.2 the center of the domain with $\eta > 0.5$ was located within the temperature range of 1085–1125 °C and at strain rates more than 0.005 s^{-1} (Fig. 14a). With an increasing in strain the first domain shifted to a higher temperature range (1090–1150°C at φ = 0.5 and 1090–1220 °C at φ = 0.7) and its strain rate range became narrower ($\dot{\varepsilon}$ = 0.006–0.08 s^{-1} at φ = 0.5 and $\dot{\varepsilon}$ = 0.03–0.1 s^{-1} at φ = 0.7) (Fig. 14b and c). The maximum value of η was 0.57 at 1100°C and $\dot{\varepsilon}$ = 0.05 s^{-1} (Fig. 14c). Another domain at φ = 0.2 was observed at temperatures higher than 1220°C for all strain rates (Fig. 14a). It shifted to higher strain rates with an increase in strain level ($\dot{\varepsilon} > 0.01$ s^{-1} at φ = 0.7) (Fig. 14b and c). The maximum value of η was 0.74 at 1250°C and $\dot{\varepsilon}$ = 0.5 s^{-1} (Fig. 14c).

The plastic flow instability region was observed at temperatures which corresponded to the $\alpha_2+\gamma$ phase field for φ = 0.2 (Fig. 14a). This is a common trend, however at greater strain (φ = 0.5) the instability region expands into the $\alpha+\gamma$ phase field at high strain rates only. In turn this phenomenon can be associated with slower both the lamellar microstructure transformation and α→γ transition at higher strain rates (Fig. 7) and, as a result, with more intensive strain localization. Due to lack of data the maps terminated beyond the plastic flow instability area showing, however, those temperature-strain areas where the specimens break (Fig. 14a, b, c). These areas extended to higher temperatures and lower strain rates with an increase in strain.

4. Discussion

The obtained results on the initial structure, phase transformations, mechanical behavior, and microstructure evolution during hot working of the Ti-43.2Al-1.9V-1.1Nb-1.0Zr-0.2Gd-0.2B alloy have revealed microstructure refinement mechanisms depending on temperature (phase fields) and allowed development of processing maps for temperatures 900–1250°C and strain rates 0.005–0.5 s^{-1} and definition of domains with the maximum efficiency of hot working.

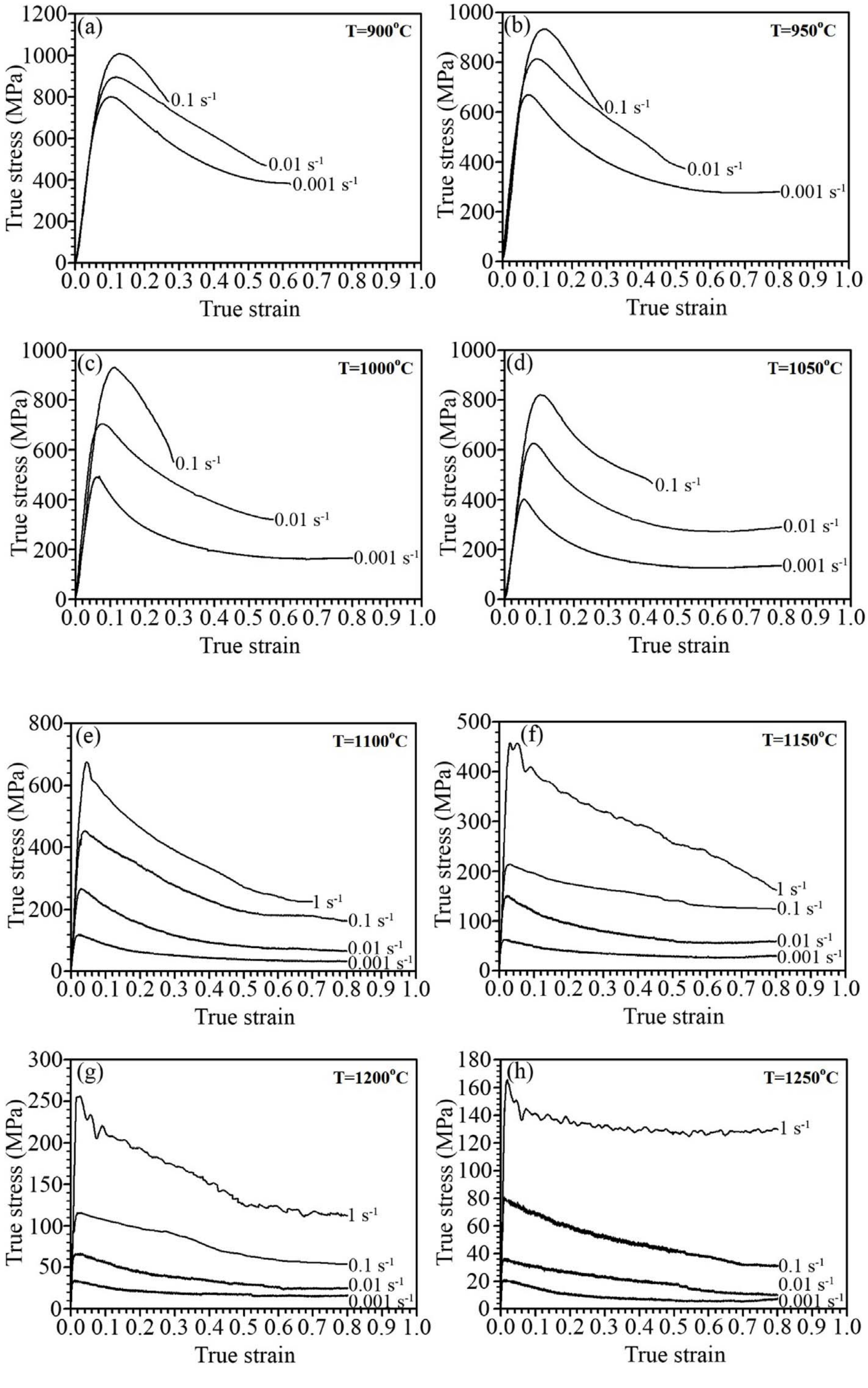

Fig. 4. True stress - true strain curves of the Ti-43.2Al-1.9V-1.1Nb-1.0Zr-0.2Gd-0.2B alloy during compression at 900 °C (a), 950 °C (b), 1000 °C (c), 1050 °C (d), 1100 °C (e); 1150 °C (f); 1200 °C (g) and 1250 °C (h). (a–e) - $\alpha_2+\gamma$ phase field; (f) - $\alpha+\gamma$ phase field; (g) - α phase field; (h) - $\alpha+\beta$ phase field.

The microstructure of the as-solidified alloy consisted of colonies of α_2/γ lamellae with the Gd aluminides, Gd oxides, borides, and the mixture of non-equilibrium β and ω phases located predominantly at the boundaries of the colonies. The fraction of the Gd-rich particles and borides was quite low besides they were located rather far from each other, most often in colony/grains boundaries. The thermodynamic modeling together with dilatometry, differential scanning calorimetry, and microstructure analysis revealed that the alloy passes the $\alpha_2+\gamma$, $\alpha+\gamma$, α, or $\alpha+\beta$ phase fields within the temperature range from 900 to 1250 °C (Fig. 2, Table 2 and Fig. 3). The phase compositions of the alloy respectively depended on temperature. The non-equilibrium phases dissolved during heating while the Gd-rich particles and borides kept almost intact within the indicated temperature interval.

Mechanical behavior (Fig. 4) has shown only moderate dependence on deformation temperature. The microstructure evolution and the post-deformation structures (Figs. 5, 6 and 9) depended on strain rate, deformation temperature and corresponding phase field, but only two temperature intervals with distinctively different behavior were found. The first one corresponded to the 900–1100 °C range, i.e. the $\alpha_2+\gamma$ phase field, where the microstructure was mainly lamellar. The second one was associated with the 1150–1250 °C range, i.e. the $\alpha+\gamma$, α, and $\alpha+\beta$ phase fields, in which the α phase dominated.

In the low-temperature interval (900–1100 °C) the alloy demonstrated typical of lamellar alloys behavior [31,32]. During plastic

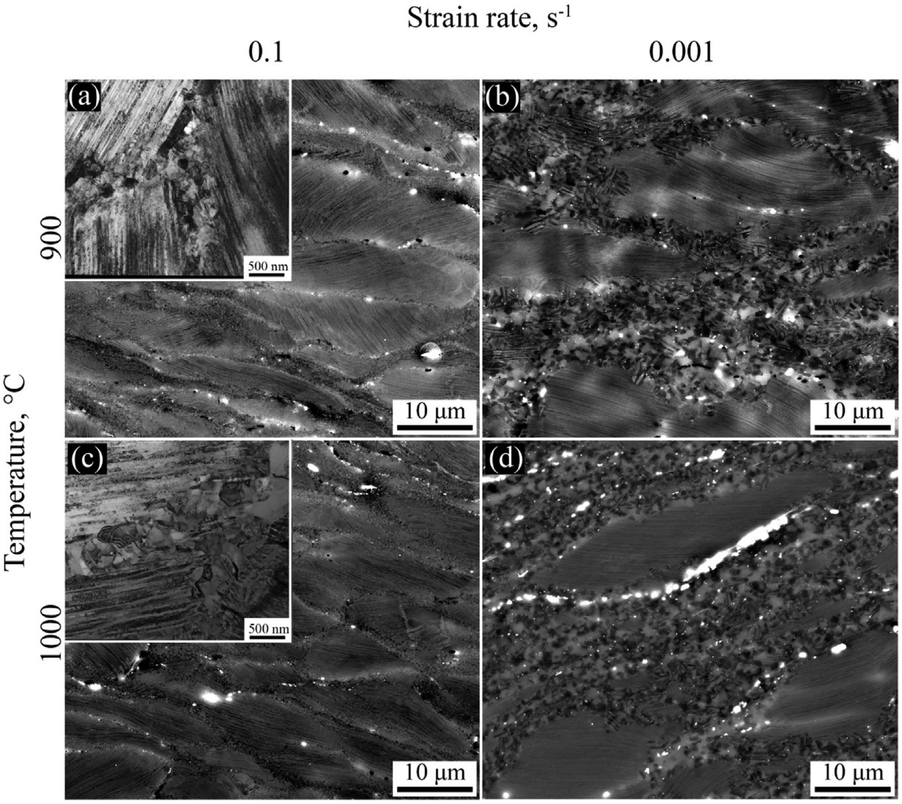

Fig. 5. Microstructure of the Ti-43.2Al-1.9V-1.1Nb-1.0Zr-0.2Gd-0.2B alloy after uniaxial compression at 900 (a, b) or 1000 °C (c, d) with a strain rate of 0.1 (a, c) or 0.001 s^{-1} (b, d) to a strain of $\varphi = 1.2$. The loading direction is vertical in all cases.

deformation a lamellar structure transformed into a globular one as a result of recrystallization/spheroidization processes in the γ and α_2 phases, thereby resulting in microstructure refinement [29]. A completely globular homogeneous microstructure with a grain size d < 3.5 µm was attained at T = 1100 °C and $\dot{\varepsilon} \le 0.01$ s^{-1} solely (Fig. 10a and b). The microstructure refinement can lead to a rather high strain rate sensitivity of the alloy ($m > 0.3$) (Table 3) and to an increase in the length of the steady state flow stage during compression tests (Fig. 4) [30,33]. Only at 1100 °C and $\dot{\varepsilon} = 0.001$ s^{-1} cracking was not observed on the side face of the specimen. Pronounced cracking at lower temperatures (Fig. 13a) was most likely associated with strain localization induced by coarse Gd-rich particles and borides.

In the second, high-temperature interval (1150–1250 °C) the alloy exhibited very similar mechanical behavior despite a pronounced difference in the phase composition of the alloy. In particular the $\alpha_2 \to \alpha$ disordering [6] and the $\gamma \to \alpha$ phase transformation (Figs. 7 and 8)

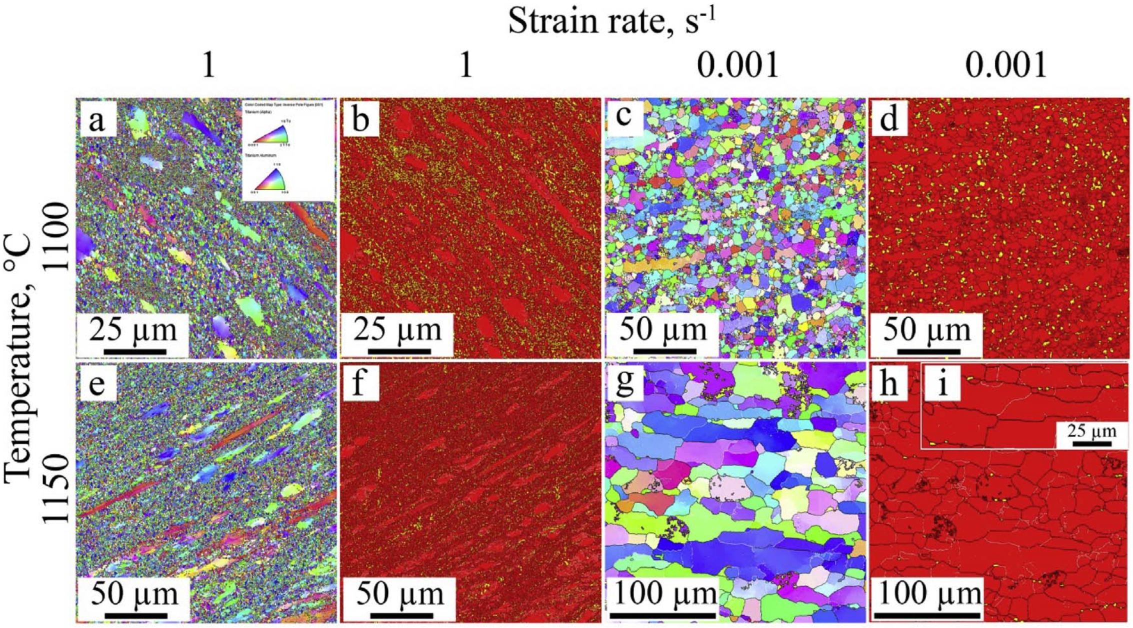

Fig. 6. EBSD inverse-pole-figures (IPF) and phase maps of the of the Ti-43.2Al-1.9V-1.1Nb-1.0Zr-0.2Gd-0.2B alloy after uniaxial compression at 1100 or 1150 °C with a strain rate of 1 or 0.001 s^{-1} to a strain of $\varphi = 1.2$. In the phase maps, the α_2/α phases are shown in red, and the γ phase – in yellow. The loading direction is vertical in all cases. (For interpretation of the references to colour in this figure legend, the reader is referred to the Web version of this article.)

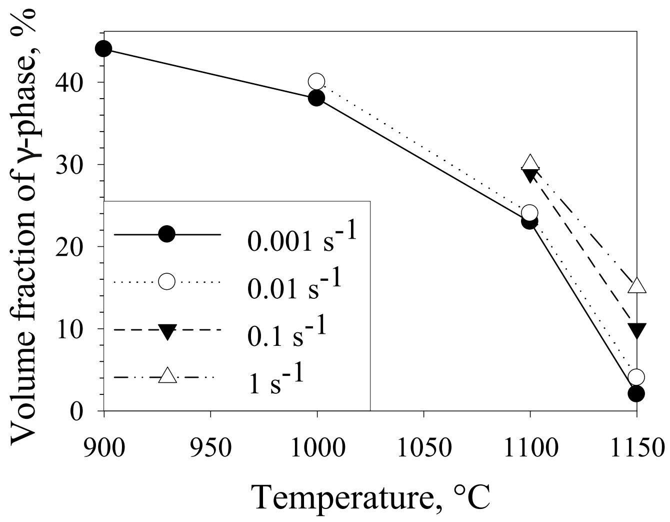

Fig. 7. Volume fraction of the γ phase in the Ti-43.2Al-1.9V-1.1Nb-1.0Zr-0.2Gd-0.2B alloy as a function of deformation temperature and strain rate. The data was obtained from the analysis of SEM-BSE images.

occurred in this temperature interval. However the contribution of dynamic recovery became more pronounced in the second temperature interval due to several factors: disordering, more active diffusion, reduction in the fraction of the γ phase and change of the phase morphology from the lamellar $\alpha_2+\gamma$ to a structure with the α phase mainly. At every temperature and at a strain rate of $\dot{\varepsilon} = 1\ \text{s}^{-1}$ the stress-strain curves showed flow stress oscillations (Fig. 4f, g, h). This phenomenon can be ascribed to dynamic recrystallization of the α phase. Although DRX in the α phase of Ti-based alloys is usually rather sluggish [34], Al decreases the stacking-fault energy [35,36] thereby increasing the kinetics of DRX [1,25,26]. An increase in deformation temperature resulted in diminishing of the oscillations. This effect can be attributed to less pronounced strain localization at higher temperatures. The DRX development resulted in considerable microstructure refinement (Fig. 10b) that promoted superplastic flow (Table 3).

The strain rate sensitivity *m* demonstrated the most pronounced dependence on a strain rate at temperatures corresponded to the $\alpha+\gamma$ and $\alpha+\beta$ phase fields. A two-phase microstructure is beneficial for the development of superplasticity because the second phase particles hinder the α phase particles coarsening. In the $\alpha+\gamma$ phase field superplasticity can be additionally promoted by the $\gamma\rightarrow\alpha$ phase transformation (Fig. 7) due to accelerated diffusion [30]. In the $\alpha+\beta$ phase field superplasticity was observed at high strain rates, so at $\dot{\varepsilon} = 0.5\ \text{s}^{-1}$ the strain rate sensitivity was $m = 0.59$. The combination of a number of factors (high deformation temperatures, small grain size, existence of soft β phase laths limiting the α grains/particles coarsening and contributing to faster diffusion) promotes SP flow of the alloy at high strain rates. It should be noted, that in spite of a small amount, the β phase was still the binder phase in the $\alpha+\beta$ phase field. The β phase created a continuous network between the dominant α particles (Fig. 12a). In two-phase titanium alloys diffusion in the β phase is faster than that in the α phase [37] and bcc β phase is softer and more ductile than the hcp α [25]. The presence of a soft diffusive layer of the β phase between hard α particles can have a favorable effect on deformation behavior as it was reported earlier for an ultrafine-grained Ti-6Al-4V alloy that showed remarkable low-temperature superplasticity [38]. In this earlier research [38] the formation of a lamellar β phase suggested extensive diffusion along boundaries between α/α particles and may be associated with the so-called "wetting" effect in the solid state [39]. A decrease in a strain rate and the formation of a coarser microstructure resulted in a decreased *m* value and suppressed superplasticity (Table 3). In our case a low fraction of the β phase laths and their heterogeneous distribution do not possibly hinder the α particles growth, as some of them reached 50–60 μm (Fig. 9h) in diameter during high-temperature compression at low strain rates. It can explain a sharp increase in the GOS < 1° fraction to 97% at 1250°C and $0.001\ \text{s}^{-1}$ (Fig. 11a). After a period of DRX development in the beginning of deformation, superplasticity become the main process controlling plastic flow; SP flow promoted grain growth thereby decreasing the fraction of low-angle boundaries. As a result the fraction of grains with the GOS < 1 reached the maximum, that is typical of completely recrystallized microstructure.

The observed mechanical behavior and microstructure evolution in

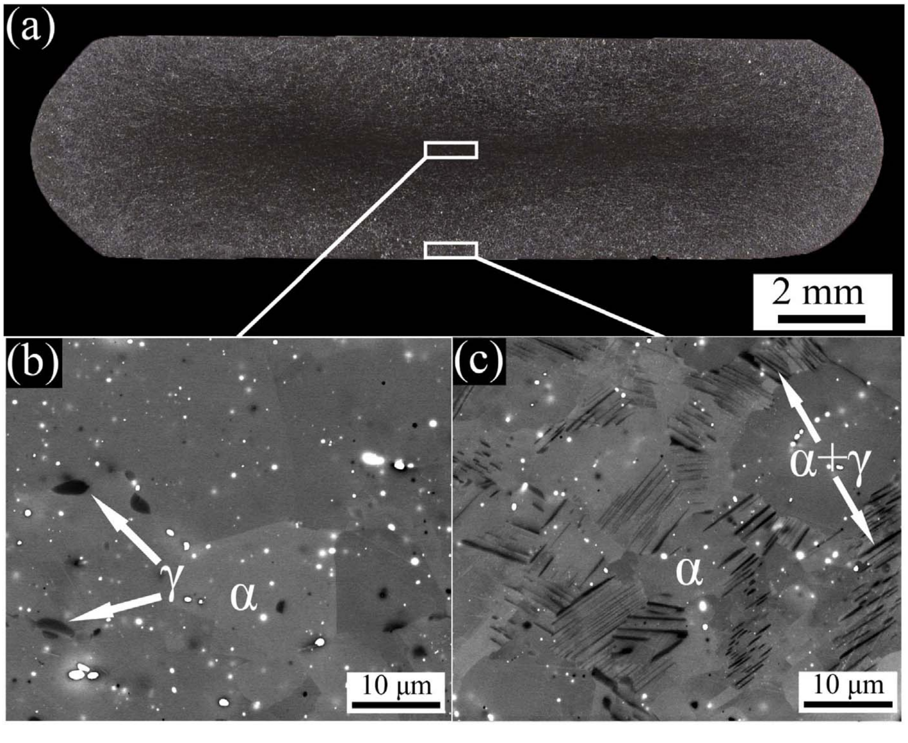

Fig. 8. Macrostructure (a) and SEM-BSE mode microstructures in different areas (b, c) of the Ti-43.2Al-1.9V-1.1Nb-1.0Zr-0.2Gd-0.2B alloy specimen deformed to $\varphi = 1.2$ at T = 1150°C, $\dot{\varepsilon} = 0.001\ \text{s}^{-1}$. The compression axis is vertical in all cases.

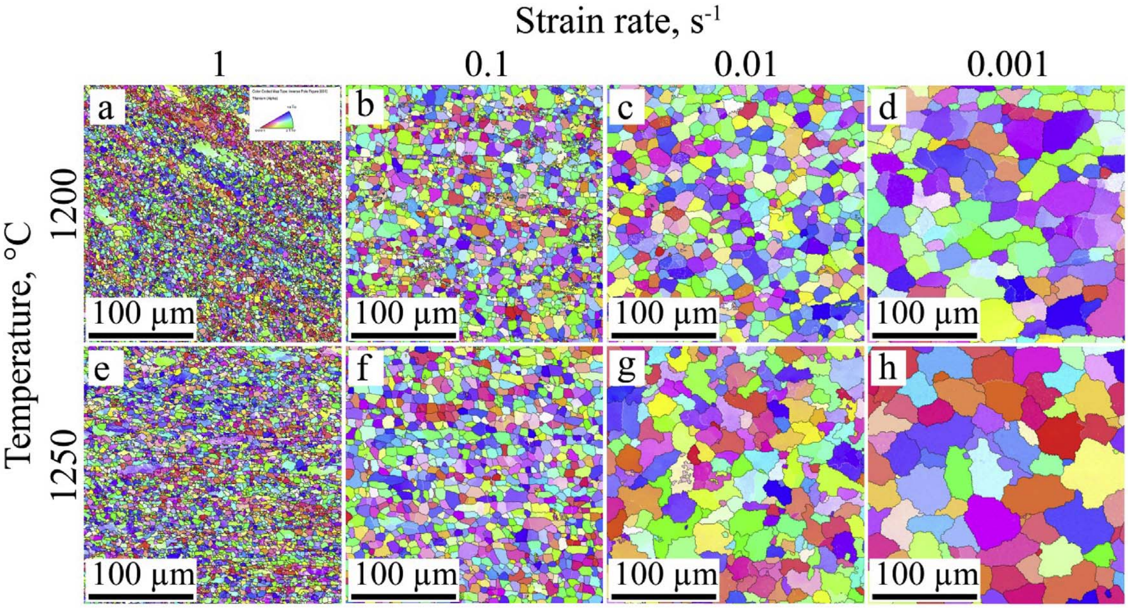

Fig. 9. EBSD IPF maps (α phase) of the Ti-43.2Al-1.9V-1.1Nb-1.0Zr-0.2Gd-0.2B alloy after uniaxial compression at 1200 °C (a–d) or 1250 °C (e–h) and strain rates of 1, 0.1, 0.01, or 0.001 s^{-1} to a strain of $\varphi = 1.2$. The loading direction is vertical in all cases.

the second temperature interval is in good agreement with the dependences of the recrystallized volume fraction (in terms of the GOS, Fig. 11a) and the HAGBs fraction (Fig. 11b) on temperature and strain rate. It is worth noting that the maximum fraction of grains with the GOS < 1° at 1150 and 1200 °C corresponded to a strain rate of 0.1 s^{-1}. The microstructure became less homogeneous at higher (Figs. 6e and f, 9a) or lower (Fig. 6g–i) strain rates that can be associated with incomplete DRX due to either (i) suppression of the process in the former case or (ii) development of dynamic recovery mainly in the latter case (Fig. 11a and b).

Due to low fraction, Gd-rich particles and borides had some influence on the microstructure evolution of the alloy at high strain rates mainly; these particles were the preferred sites for cracks and pores nucleation (Fig. 13). Meanwhile, the segregation of oxygen to Gd_2TiO_5 oxides have most likely a positive effect on ductility of the alloy since dissolved oxygen can decrease ductility of the γ TiAl based alloys [17]. The obtained data does not suggest any noticeable effect of Gd-rich and boride particles on dynamic recrystallization and recovery. They do not serve as the preferred sites for low/high angle boundaries formation, although probably can limit the dislocation mobility.

The processing maps for the Ti-43.2Al-1.9V-1.1Nb-1.0Zr-0.2Gd-0.2B alloy (Fig. 14) summarized the obtained results on mechanical behavior and structure evolution. Domains corresponding to superplastic deformation with power dissipation efficiency $\eta = 0.5$ [3] at $\varphi = 0.2$ were found in the $\alpha_2+\gamma$, $\alpha+\gamma$ and $\alpha+\beta$ phase fields (Fig. 14a). Superplastic flow was preceded by the microstructure refinement due to development of either DRX/spheroidization processes in the $\alpha_2+\gamma$ phase field or DRX in the $\alpha+\gamma$, α and $\alpha+\beta$ phase fields. These processes are observed on the processing maps at $\eta = 0.3$ in accordance with [3] and are bounded by the area of unstable flow (Fig. 14a, b, c). With an increase in strain this bound moved towards increasing the strain rate interval of DRX/spheroidization in the $\alpha_2+\gamma$ phase field. This observation is in agreement with an increase in both the recrystallized/spheroidized volume and the length of the steady-state flow stage at higher strain rates (Figs. 4a–e, 5, 6a and c, 10a). Domains which corresponded to SP flow (where both the microstructure refinement is the most efficient and the recrystallized volume grows faster, Figs. 10a and b; 11a, b; 14a, b, c) gradually became wider. That is why the processing map for $\varphi = 0.7$ shows a trend towards merging of areas with $\eta > 0.5$ (Fig. 14c); however areas with the maximum efficiency can still be determined.

Similar locations of areas with the maximum efficiency were observed on the processing maps for a TNM-B_1 alloy obtained at higher temperatures [9]. However instead of SP domains the authors of [9] registered DRX areas. The difference between the present data and the results reported in Ref. [9] can be associated with some variation in the phase composition (the stable β phase exists in TNM-B_1 alloy as a result of alloying within the whole investigated temperature interval (1150–1300°C) while the α phase field was not found). Dynamic recrystallization can be observed in both the TNM-B_1 and Ti-43.2Al-1.9V-

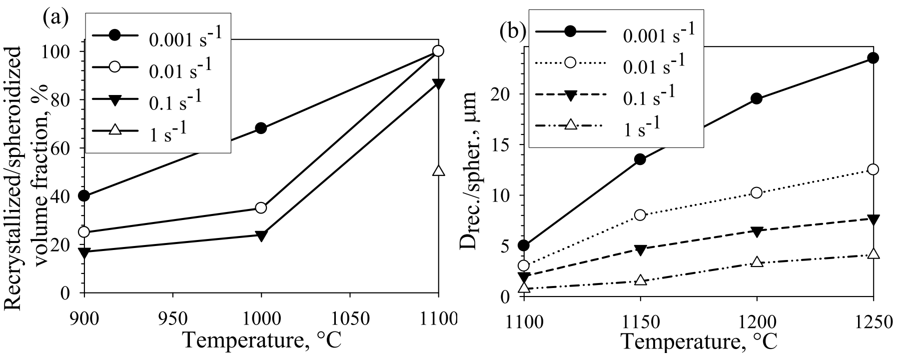

Fig. 10. Volume fraction (a) and size (b) of recrystallized/spheroidized grains in the Ti-43.2Al-1.9V-1.1Nb-1.0Zr-0.2Gd-0.2B alloy as a function of deformation temperature and strain rate. The data was obtained from the analysis of SEM-BSE images.

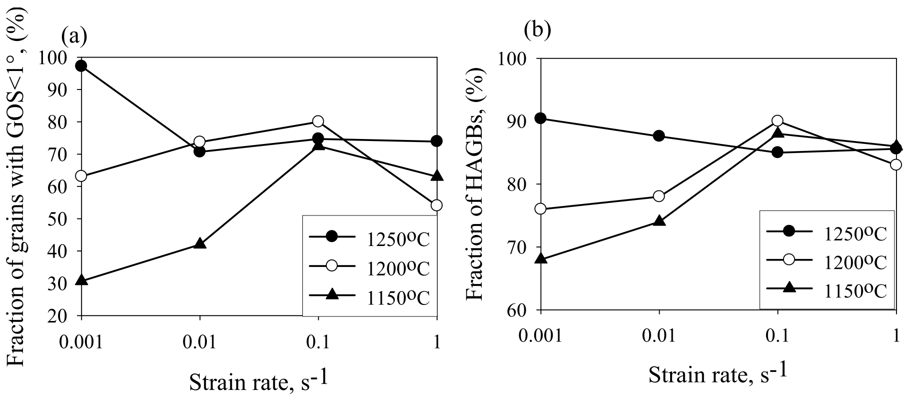

Fig. 11. Dependence of the volume fraction of grains with the GOS < 1° (a) and the HAGBs fraction (b) calculated from the EBSD data for deformation temperatures of 1150–1250°C and strain rates of 0.001–1 s^{-1}.

1.1Nb-1.0Zr-0.2Gd-0.2B alloys in the $\alpha_2+\gamma+\beta$, $\alpha+\gamma+\beta$, $\alpha+\beta$ and $\alpha_2+\gamma$, $\alpha+\gamma$, α phase fields, respectively. However, for instance, superplasticity in the $\alpha+\beta$ phase field was not indicated in the TNM-B_1 despite high values of power dissipation efficiency ($\eta > 0.6$). This phenomenon can be associated with low fraction of the recrystallized microstructure even at $\varphi = 0.9$. By contrast, the uniform equiaxed fine-grain structure formed during deformation of the Ti-43.2Al-1.9V-1.1Nb-1.0Zr-0.2Gd-0.2B alloy in the $\alpha+\beta$ phase field at $\dot{\varepsilon} = 1\ s^{-1}$ thereby promoting the development of superplastic flow.

Rather unusual finding is associated with the terminating of the processing maps beyond the flow instability region due to lower ductility of the alloy in comparison with other TiAl based alloys, especially in the $\alpha_2+\gamma$ phase field and at high strain rates (Fig. 14a, b, c). Similar results were not observed in earlier works [6–10,25,31,32]. The presence of Gd-rich and boride particles appreciably reduces the workability of the alloy in the $\alpha_2+\gamma$ phase field and at high strain rates thereby shifting processing temperatures to the top of the $\alpha+\gamma$, α and $\alpha+\beta$ phase fields and to lower strain rates.

5. Conclusions

1. The microstructure of as-cast Ti-43.2Al-1.9V-1.1Nb-1.0Zr-0.2Gd-0.2B alloy consisted of lamellar $\alpha_2+\gamma$ colony structure; the γ, β and ω phase particles were located at colony boundaries. Besides two types of Gd-rich phases (Gd_3Al and Gd_2TiO_5) and two types of borides (TiB and TiB_2) were found inside colonies and their boundaries. The following phase fields by Thermo-Calc modeling and experimental investigations of structure evolution during heating were revealed: ($\alpha_2+\gamma$), ($\alpha+\gamma$), (α), ($\alpha+\beta$).
2. Two temperature intervals with different mechanical behavior were found: the first one was corresponded to the $\alpha_2+\gamma$ phase field (900–1100 °C), where the microstructure had mainly a lamellar morphology, and the second interval comprised the $\alpha+\gamma$, α, and $\alpha+\beta$ phase fields (1150–1250 °C), in which the α phase dominated. In the first interval, mechanical behavior was typical of a lamellar structure and was associated with the transformation of the lamellar structure into globular one. In the second interval, mechanical behavior was similar despite changes in phase composition.

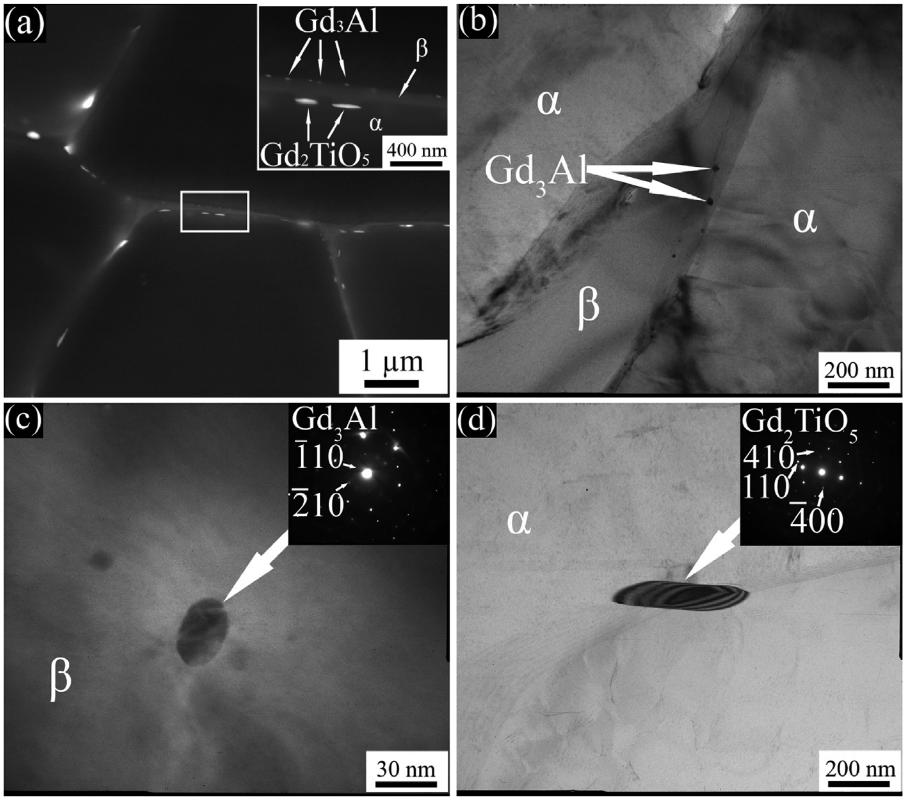

Fig. 12. Microstructure of the Ti-43.2Al-1.9V-1.1Nb-1.0Zr-0.2Gd-0.2B alloy specimens deformed to $\varphi = 1.2$ at T = 1250 °C and $\dot{\varepsilon} = 0.001\ s^{-1}$: (a) overview at low and high magnification; (b) Gd_2TiO_5 and $GdAl_3$ phases particles in a α/β boundary; (c) a $GdAl_3$ phase particle in a β lamella; (d) a Gd_2TiO_5 phase particle in a boundary between α grains; (a) SEM-BSE images; (c–d) bright-field TEM images. SAED patterns are shown for the corresponding precipitates. The compression axis is vertical in all cases.

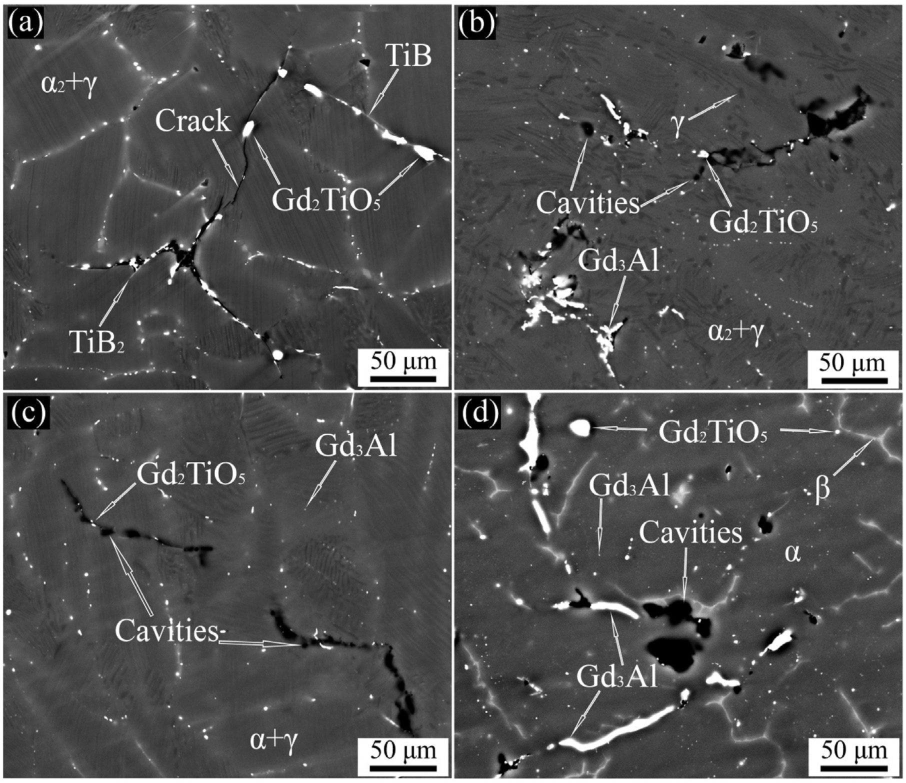

Fig. 13. SEM image of cracking at colony/grain boundaries of the Ti-43.2Al-1.9V-1.1Nb-1.0Zr-0.2Gd-0.2B alloy occurring the side faces of the specimens deformed to $\varphi = 1.2$ at: (a) T = 900°C $\dot{\varepsilon} = 0.001\ s^{-1}$, (b) T = 1100 °C $\dot{\varepsilon} = 0.001\ s^{-1}$, (c) T = 1150 °C $\dot{\varepsilon} = 1\ s^{-1}$ and (d) T = 1250°C, $\dot{\varepsilon} = 1\ s^{-1}$. The compression axis is vertical in all cases.

Oscillations of stress-strain curves were observed in $(\alpha+\gamma)$, (α) and $(\alpha+\beta)$ phase fields at a strain rate of 1 s^{-1}. In both intervals mechanical behavior was complicated by Gd-rich phases and borides particles, which promoted strain localization and cracking.

3. It was found that deformation in both intervals resulted in microstructure refinement; the refined microstructure fraction increased with an increasing in temperature and a decreasing in a strain rate in the $(\alpha_2+\gamma)$ phase field due to spheroidization/dynamic

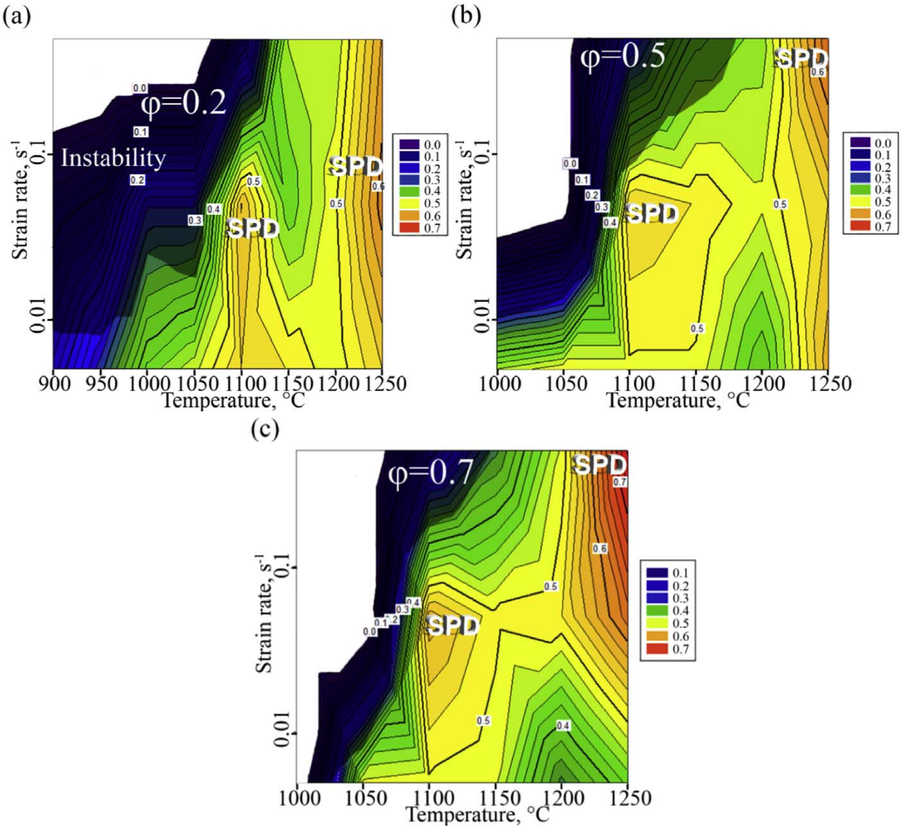

Fig. 14. Processing map of the Ti-43.2Al-1.9V-1.1Nb-1.0Zr-0.2Gd-0.2B alloy at a true strain $\varphi = 0.2$ (a), 0.5 (b) and 0.7 (c). Isolines indicate the power dissipation efficiency (η).

Table 3
Dependence of the strain rate sensitivity of flow stress (*m*) of the Ti-43.2Al-1.9V-1.1Nb-1.0Zr-0.2Gd-0.2B alloy on strain, deformation temperature and strain rate.

Temperature, °C	$\dot{\varepsilon}$, s^{-1}	Strain rate sensitivity of flow stress *m* at different strains		
		$\varphi = 0.2$	$\varphi = 0.5$	$\varphi = 0.7$
900	0.05	0.04	–	-
	0.005	0.09	–	–
950	0.05	0.06	–	–
	0.005	0.17	–	–
1000	0.05	0.16	–	–
	0.005	0.28	0.29	–
1050	0.05	0.16	–	–
	0.005	0.31	0.33	0.32
1100	0.5	0.09	0.14	0.10
	0.05	0.39	0.37	0.40
	0.005	0.37	0.33	0.33
1150	0.5	0.30	0.26	0.20
	0.05	0.27	0.35	0.34
	0.005	0.35	0.33	0.32
1200	0.5	0.30	0.29	0.32
	0.05	0.33	0.32	0.35
	0.005	0.32	0.25	0.20
1250	0.5	0.34	0.47	0.59
	0.05	0.36	0.37	0.46
	0.005	0.39	0.40	0.27

recrystallization processes. In the ($\alpha+\gamma$), (α) and ($\alpha+\beta$)-phase fields the development of microstructure was associated with dynamic recrystallization mainly. The refined microstructure volume weakly depended on deformation temperature and was maximum at the strain rate of 0.1 s^{-1}.

4. It was shown that the $\gamma\rightarrow\alpha$ transformation occurred more intensively during deformation in ($\alpha+\gamma$)-phase field (T = 1150 °C, $\dot{\varepsilon} = 0.001$ s^{-1}, $\varphi = 1.2$) in comparison to soak at the same temperature. The difference in the kinetics of the $\gamma\rightarrow\alpha$ transformation decreased with an increase in a strain rate.
5. Processing maps of the Ti-43.2Al-1.9V-1.1Nb-1.0Zr-0.2Gd-0.2B alloy in the as-cast condition for the temperature interval from 900 to 1250 °C; strain rates from 0.001 to 1 s^{-1} and $\varphi = 0.2$; 0.5; 0.7 was constructed. Two domains with high power dissipation efficiency ($\eta > 0.5$) were observed: the first domain was in the ($\alpha_2+\gamma$) and ($\alpha+\gamma$) phase fields with the peak efficiency of 0.57 at ~1100 °C and 0.05 s^{-1}. The second domain belonged to the $\alpha+\beta$ phase field with the maximum efficiency of 0.74 at ~1250 °C and 0.5 s^{-1}. Due to lack of data the processing maps terminated beyond the plastic flow instability area showing, however, temperature-strain areas where the specimens break.

Acknowledgment

The work was financially supported by Russian Foundation for Basic Research, grant № 16-08-01061. The authors are grateful to the personnel of the Joint Research Center, “Technology and Materials”, Belgorod State National Research University, for their assistance with the instrumental analysis.

Appendix A. Supplementary data

Supplementary data related to this article can be found at http://dx.doi.org/10.1016/j.intermet.2018.01.004.

References

[1] F. Appel, J.D.H. Paul, M. Oehring, Gamma Titanium Aluminide Alloys: Science and Technology, Wiley, Weinheim, 2012.

[2] H. Clemens, S. Mayer, Design, processing, microstructure, properties, and applications of advanced intermetallic TiAl alloys, Adv. Eng. Mater. 15 (2013) 191–215, http://dx.doi.org/10.1002/adem.201200231.

[3] Y.V.R.K. Prasad, S. Sasidhara (Eds.), Hot Working Guide: a Compendium of Processing Maps, ASM International, Materials Park, OH, 1997.

[4] R.M. Imayev, V.M. Imayev, M. Oehring, F. Appel, Microstructural evolution during hot working of Ti aluminide alloys: influence of phase constitution and initial casting texture, Metall. Mater. Trans. A Phys. Metall. Mater. Sci. 36 (2005) 859–867, http://dx.doi.org/10.1007/s11661-005-1015-1.

[5] V.T. Witusiewicz, A.A. Bondar, U. Hecht, T.Y. Velikanova, The Al-B-Nb-Ti system. IV. Experimental study and thermodynamic re-evaluation of the binary Al-Nb and ternary Al-Nb-Ti systems, J. Alloy. Comp. 472 (2009) 133–161, http://dx.doi.org/10.1016/j.jallcom.2008.05.008.

[6] F. Kong, Y. Chen, D. Zhang, S. Zhang, High Temperature Deformation Behavior of Ti – 46Al – 2Cr – 4Nb – 0. 2Y Alloy vol. 539, (2012), pp. 107–114, http://dx.doi.org/10.1016/j.msea.2012.01.066.

[7] J.H. Kim, Y.W. Chang, C.S. Lee, T. Kwon Ha, High-temperature deformation behavior of a gamma TiAl alloy—microstructural evolution and mechanisms, Metall. Mater. Trans. 34 (2003) 2165–2176, http://dx.doi.org/10.1007/s11661-003-0280-0.

[8] G. Wang, L. Xu, Y. Wang, Z. Zheng, Y. Cui, R. Yang, Processing maps for hot working behavior of a PM TiAl alloy, J. Mater. Sci. Technol. 27 (2011) 893–898, http://dx.doi.org/10.1016/S1005-0302(11)60161-8.

[9] E. Schwaighofer, H. Clemens, J. Lindemann, A. Stark, S. Mayer, Hot-working behavior of an advanced intermetallic multi-phase??-TiAl based alloy, Mater. Sci. Eng. 614 (2014) 297–310, http://dx.doi.org/10.1016/j.msea.2014.07.040.

[10] S. Zeng, A. Zhao, H. Jiang, Y. Ren, Flow behavior and processing maps of Ti-44.5Al-3.8Nb-1.0Mo-0.3Si-0.1B alloy, J. Alloy. Comp. 698 (2017) 786–793, http://dx.doi.org/10.1016/j.jallcom.2016.12.214.

[11] L. Song, X.J. Xu, L. You, Y.F. Liang, J.P. Lin, Phase transformation and decomposition mechanisms of the βo(ω) phase in cast high Nb containing TiAl alloy, J. Alloy. Comp. 616 (2014) 483–491, http://dx.doi.org/10.1016/j.jallcom.2014.07.130.

[12] A. Stark, E. Schwaighofer, S. Mayer, H. Clemens, T. Lippmann, L. Lottermoser, A. Schreyer, F. Pyczak, In situ high-energy XRD study of the hot-deformation behavior of a novel γ-TiAl alloy, Mater. Res. Soc. Symp. Proc. 1 (2012) 71–76, http://dx.doi.org/10.1557/opl.2012.1577.

[13] E.N. Kablov, N.A. Nochovnaya, D.E. Kablov, V.V. Antipov, P.V. Panin, A.S. Kochetkov, Alloy based on titanium intermetallic compound and an product made of it, Russian patent RU 2606368 C1. (2017).

[14] H. Zhou, Y. Zhan, J. Yan, S. Yuan, Phase relationship in the Gd-Ti-Al ternary system at 500°C, J. Mater. Sci. 37 (6) (2002) 1203–1205, http://dx.doi.org/10.1023/A:101437570.

[15] J. Zhang, D. Feng, F.J. Yin, Some new aspects in developing TiAl based alloys as competitive high temperature materials, Adv. Mater. Res. 278 (2011) 557–562, http://dx.doi.org/10.4028/www.scientific.net/AMR.278.557.

[16] C. Liu, K. Xia, W. Li, The comparison of effects of four rare earth elements additions on structures and grain sizes of Ti-44Al alloy, J. Mater. Sci. 37 (2002) 1515–1522, http://dx.doi.org/10.1023/A:1014900325485.

[17] Y.Y. Chen, B.H. Li, F.T. Kong, Microstructural refinement and mechanical properties of Y-bearing TiAl alloys, J. Alloy. Comp. 457 (2008) 265–269, http://dx.doi.org/10.1016/j.jallcom.2007.03.050.

[18] Standard Test Method for Determining Volume Fraction by Systematic Manual Point Count, ASTM E562 – 11. doi:10.1520/E0562-11.

[19] H.Z. Niu, Y.Y. Chen, F.T. Kong, J.P. Lin, Microstructure evolution, hot deformation behavior and mechanical properties of Ti-43Al-6Nb-1B alloy, Intermetallics 31 (2012) 249–256, http://dx.doi.org/10.1016/j.intermet.2012.07.016.

[20] http://crystdb.nims.go.jp.

[21] M.A. Petrova, A.S. Novikova, R.G. Grebenshchikov, Phase relations in the pseudobinary systems La_2TiO_5–Lu_2TiO_5 and Gd_2TiO_5–Tb_2TiO_5, Inorg. Mater. 39 (5) (2003) 509–513, http://dx.doi.org/10.1023/A:1023628812895 Translated from Neorganicheskie Materialy, Vol. 39, No. 5, 2003, pp. 609–613.

[22] M. Schloffer, B. Rashkova, T. Schöberl, E. Schwaighofer, Z. Zhang, H. Clemens, S. Mayer, Evolution of the ω_o phase in a β-stabilized multi-phase TiAl alloy and its effect on hardness, Acta Mater. 64 (2014) 241–252, http://dx.doi.org/10.1016/j.actamat.2013.10.036.

[23] M. Schloffer, F. Iqbal, H. Gabrisch, E. Schwaighofer, F.P. Schimansky, S. Mayer, A. Stark, T. Lippmann, M. Göken, F. Pyczak, H. Clemens, Microstructure development and hardness of a powder metallurgical multi phase γ-TiAl based alloy, Intermetallics 22 (2012) 231–240, http://dx.doi.org/10.1016/j.intermet.2011.11.015.

[24] G.E. Bean, M.S. Kesler, M.V. Manuel, Effect of Nb on phase transformations and microstructure in high Nb titanium aluminides, J. Alloy. Comp. 613 (2014) 351–356, http://dx.doi.org/10.1016/j.jallcom.2014.05.092.

[25] B. Liu, Y. Liu, Y.P. Li, W. Zhang, A. Chiba, Thermomechanical characterization of β-stabilized Ti-45Al-7Nb-0.4W-0.15B alloy, Intermetallics 19 (2011) 1184–1190, http://dx.doi.org/10.1016/j.intermet.2011.03.021.

[26] F.J. Humphreys, M. Hatherly, Recrystallization and Related Annealing Phenomena, Elsevier, Oxford, 2004.

[27] G.A. Salishchev, O.N. Senkov, R.M. Imayev, V.M. Imayev, M.R. Shagiev, A. V Kuznetsov, F. Appel, M. Oehring, O.A. Kaibyshev, F.H. Froes, Processing and deformation behavior of gamma TiAl alloys with fine-grained equiaxed microstructures, Adv. Perform. Mater. 6 (1999) 107–116, http://dx.doi.org/10.1023/A:1008718724229.

[28] H.Z. Niu, Y.Y. Chen, S.L. Xiao, F.T. Kong, C.J. Zhang, High temperature deformation behaviors of Ti-45Al-2Nb-1.5V-1Mo-Y alloy, Intermetallics 19 (2011) 1767–1774, http://dx.doi.org/10.1016/j.intermet.2011.07.025.

[29] G.A. Salishchev, R.M. Imayev, O.N. Senkov, V.M. Imayev, N.K. Gabdullin, M.R. Shagiev, A.V. Kuznetsov, F.H. Froes, Formation of a submicrocrystalline

structure in TiAl and Ti3Al intermetallics by hot working, Mater. Sci. Eng. 286 (2000) 236–243, http://dx.doi.org/10.1016/S0921-5093(00)00806-6.

[30] O.A. Kaibyshev, Superplasticity in Alloys, Intermetallics and Ceramics, Springer-Verlag, Berlin, 1992.

[31] H. Zhou, F. Kong, X. Wang, Y. Chen, Hot deformation behavior and microstructural evolution of as-forged Ti-44Al-8Nb- (W, B, Y) alloy with nearly lamellar microstructure, Intermetallics 81 (2017) 62–72, http://dx.doi.org/10.1016/j.intermet.2017.02.026.

[32] N. Cui, F. Kong, X. Wang, Y. Chen, H. Zhou, Hot deformation behavior and dynamic recrystallization of a β -solidifying TiAl alloy, Mater. Sci. Eng. 652 (2016) 231–238, http://dx.doi.org/10.1016/j.msea.2015.11.097.

[33] R.M. Imayev, O.A. Kaibyshev, G.A. Salishchev, Mechanical behavior of fine grained TiAl intermetallic compound-I. Superplasticity, Acta Metall. 40 (1992) 581–587, http://dx.doi.org/10.1016/0956-7151(92)90407-6.

[34] G.A. Salishchev, R.M. Galeev, O.R. Valiakhmetov, Dynamic Recrystallization of Titanium, Izv. Ross. Akad. Nauk, Met. No. 1, (1994), pp. 125–129.

[35] A. Fitzner, D.G.L. Prakash, J.Q. Da Fonseca, M. Thomas, S.Y. Zhang, J. Kelleher, P. Manuel, M. Preuss, The effect of aluminium on twinning in binary alpha-titanium, Acta Mater. 103 (2016) 341–351, http://dx.doi.org/10.1016/j.actamat.2015.09.048.

[36] Z. Guo, A.P. Miodownik, N. Saunders, J.P. Schillé, Influence of stacking-fault energy on high temperature creep of alpha titanium alloys, Scr. Mater 54 (2006) 2175–2178, http://dx.doi.org/10.1016/j.scriptamat.2006.02.036.

[37] Y. Mishin, C. Herzig, Diffusion in the Ti–Al system, Acta Mater. 48 (2000) 589–623, http://dx.doi.org/10.1016/S1359-6454(99)00400-0.

[38] S.V. Zherebtsov, E.A. Kudryavtsev, G.A. Salishchev, B.B. Straumal, S.L. Semiatin, Microstructure evolution and mechanical behavior of ultrafine Ti-6Al-4V during low-temperature superplastic deformation, Acta Mater. 121 (2016) 152–163, http://dx.doi.org/10.1016/j.actamat.2016.09.003.

[39] G.A. López, E.J. Mittemeijer, B.B. Straumal, Grain boundary wetting by a solid phase; microstructural development in a Zn-5 wt% Al alloy, Acta Mater. 52 (2004) 4537–4545, http://dx.doi.org/10.1016/j.actamat.2004.06.011.